ADVANCED FUNCTIONAL MATERIALS

Supporting Information

for *Adv. Funct. Mater.*, DOI: 10.1002/adfm.201909904

$CsPbBr_3$ Nanocrystal Films: Deviations from Bulk Vibrational and Optoelectronic Properties

*Silvia G. Motti, Franziska Krieg, Alexandra J. Ramadan, Jay B. Patel, Henry J. Snaith, Maksym V. Kovalenko, Michael B. Johnston, and Laura M. Herz**

Supporting Information

$CsPbBr_3$ nanocrystal films: deviations from bulk vibrational and optoelectronic properties

Silvia G. Motti,[1] Franziska Krieg,[2,3] Alexandra J. Ramadan,[1] Jay B. Patel,[1] Henry J. Snaith,[1] Maksym V. Kovalenko,[2,3] Michael B. Johnston,[1] Laura M. Herz[1]

Contents

1 Sample Preparation

1.1 Chemicals

The following reagents were purchased and used as received:

Cs_2CO_3 and 1,3-propanesultone were purchased from Fluorochem, lead acetate trihydrate (99.99%), bromine (99.9%), 1-octadecene (ODE, technical grade), 3-(N,N-dimethyloctadecylammonio)propanesulfonate (>99% , Ligand 1), ethylacetate (HPLC grade ≥99.7%) and oleic acid (90%, OA) hexamethyldisilazane (99.9%, HMDS), hexamethylenediamine (98%), formic acid (98%), potassium hydroxide (ACS reagent grade), sodium sulfate (99.0% anhydrous), acetone (99.5%), dimethyl sulfoxide (anhydrous, ≥99.9%) from Sigma Aldrich/Merck, toluene (for synthesis) and acetone (HPLC grade), formaldehyde (37-41% in water), diethyl ether (ACS reagent grade) from Fischer and trioctylphosphine (>97%, TOP) and oleylamine (>95%, OLA) from STREM. soy-lecithin (>97%, biochemistry grade, ligand 2) from Roth. Cesium bromide (99.9 % metals basis) and lead bromide (98% +) from Alfa Aesar and chloroform (≥99.8%, contains 0.5-1.0% ethanol as stabilizer) from Honeywell Riedel-de Haen.

The following compounds were prepared as described and characterized below:

1.1.1 Cs-oleate 0.4 M in ODE.

Cesium carbonate (1.628 g, 5 mmol), oleic acid (5 mL, 16 mmol) and 1-octadecene (20 mL) were evacuated at 25-120 °C until the completion of gas evolution.

1.1.2 Pb-oleate 0.5 M in ODE.

Lead (II) acetate trihydrate (4.607g, 12 mmol), oleic acid (7.6 mL, 24 mmol) and 1-octadecene (16.4 mL) were mixed in a three-necked flask and evacuated at 25-120 °C until the complete evaporation of acetic acid and water.

1.1.3 TOP-Br_2 0.5 M in toluene.

TOP (6mL, 13 mmol) and bromine (0.6 mL, 11.5 mmol) were mixed under inert atmosphere. Once the reaction was complete and cooled to room temperature, the TOP-Br_2 was dissolved in toluene (18.7 mL).

1.1.4 Synthesis of "ligand 3" (3,3'-(hexane-1,6-diylbis(dimethylammoniumdiyl))bis propane-1-sulfonate)

1.1.4.1 Step 1: Synthesis of N,N, N, N-tetramethyl hexane-1,6-diamine (1)

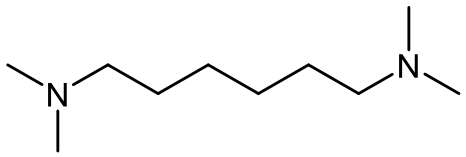

1

N,N, N, N-tetramethyl hexane-1,6-diamine

N,N, N, N-tetramethyl hexane-1,6-diamine was synthesized following a procedure published in [1].

Hexamethylenediamine (5.4 g, 53 mmol) was dissolved in formaldehyde (10 mL) and formic acid (10 mL) was added dropwise over the course of 1 h. The mixture was heated to reflux at 80°C and kept at this temperature for 8 h. A viscous slightly yellow crude solution results. The pH was rendered basic by addition of 10% KOH and the product was extracted using 3 x 50 mL diethylether. The combined organic phases were dried over Na_2SO_4 and the solvent was removed in vacuo. The so received oil was further purified by fractional distillation under reduced pressure. The product, a clear oil, was obtained at 10^{-2} mbar, 30°C.

Yield: 2.417 g, 14 mmol, 26%, **1**

^{1}H-NMR: (300 MHz, $CDCl_3$) δ = 2.175 (t, 4H), 2.14 (s, 12H), 1.40 (m, 4 H), 1.26 (m, 4H)

^{13}C-NMR: (75 MHz, $CDCl_3$) δ = 59.89, 45.44, 27.67, 27.44 ppm

1.1.4.2 Step 2: Synthesis of 3,3'-(hexane-1,6-diylbis(dimethylammoniumdiyl))bis propane-1-sulfonate (2)

1 (2.417 g, 14 mmol, 1Eq) and 1,3-propanesultone (4.5465 g, 37 mmol, 2.6 Eq) were mixed in acetone (40 mL) and stirred at room temperature for 12 hours. The product formed as a white precipitate and was isolated by vacuum filtration. The product is a white hygroscopic powder.

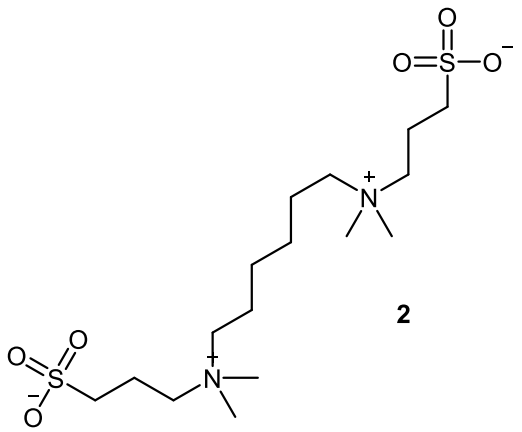

2

3,3'-(hexane-1,6-diylbis(dimethylammoniumdiyl))bis(propane-1-sulfonate)

^{1}H-NMR: (300 MHz, DMSO d^{6}) δ = 3.42 (m, 4 H), 3.25 (m, 4 H), 3.02 (s, 12 H), 2.48 (t, 4H), 1.97 (m, 4 H), 1.71 (b, 4 H), 1.34 (b, 4 H) ppm

^{13}C-NMR: (75 MHz, DMSO d^{6}) δ = 62.31, 61.82, 50.28, 47.47, 24.84, 20.91, 18.85 ppm

1.2 $CsPbBr_3$ Nanocrystal synthesis and purification

1.2.1 Synthesis of $CsPbBr_3$ NCs with ligand 1

Cesium lead bromide nanocrystals were synthesized in an up-scaled version of our previously published procedure.[2] Lead-oleate (5 mL, 0.5M, 0.025 mol), Cs-oleate (4 mL, 0.4M, 0.016 mol), ligand 1(0.215g, 0.5 mmol) and ODE (10 mL) were combined in a 50 mL three-necked-flask and heated to 120°C under vacuum. Once the gas evolution stopped, the atmosphere was changed to argon and the mixture was heated to the reaction temperature (100 °C for 6 nm NCs, 130 °C for 7.5 nm NCs and 180 °C for 10 nm NCs). Once the reaction temperature was reached, TOP-Br_2 (5 mL, 0.5M, 0.025 mol) was injected and the reaction was cooled immediately in an ice-bath.

Purification

10 nm NCs

The turbid crude solution was centrifuged at 12 krpm (29500 g) for 10 minutes at 17 °C, the supernatant was discarded and the precipitate dispersed in toluene (10 mL). Subsequently the NCs were purified from excess ligands and synthesis byproducts by repeated (3 times) precipitation with ethylacetate (2 volumetric equivalents) and centrifugation at 12 krpm for 1 minute at 17 °C and dispersion in toluene. The solvent volume was reduced by factor of two in each washing step. 3 mL of toluene were used for the last dispersion. The final concentration of the colloidal solution was 88 mg/mL (core mass/solvent volume), as determined by optical absorption measurements.[3]

6 and 7.5 nm NCs

These crude solutions were clear (not turbid). The crude solution (24 mL) was centrifuged at 12 krpm (29500 g) for 10 minutes at 17°C. The precipitate, if any was present, was discarded and the supernatant was precipitated with 50 mL of ethyl acetate and centrifugation at 12 krpm (29500 g) for 10 minutes at 17°C. The precipitate was dispersed in 10 mL of toluene. Subsequently the NCs were purified from excess ligands and synthesis byproducts by repeated (3 times) precipitation with ethylacetate (2 volumetric equivalents) and centrifugation at 12 krpm for 1 minute at 17°C and dispersion in toluene. The solvent volume was reduced by factor 2 in each washing step. For the last dispersion 3 mL of toluene were used. The final concentration of the colloidal solutions were 36 mg/mL for the 6 nm NCs and 106 mg/mL for the 7.5 nm NCs respectively.

1.2.2 Synthesis of $CsPbBr_3$ NCs with ligand 2

Cesium lead bromide nanocrystals were synthesized in a modified version of our previously published procedure.[4] Lead-oleate (5 mL, 0.5M, 0.025 mol), Cs-oleate (4 mL, 0.4M, 0.016 mol), ligand 2 (1.5522 g, 1.9 mmol) and ODE (10 mL) were combined in a 50 mL three-

necked-flask and heated to 120°C under vacuum. Once the gas evolution stopped, the atmosphere was changed to argon and the mixture was heated to 130°C. Once the reaction temperature was reached, TOP-Br_2 (5 mL, 0.5M, 0.025 mol) was injected and the reaction was cooled immediately in an ice-bath.

The crude solution (24 mL) was centrifuged at 12 krpm (29500 g) for 10 minutes at 17°C. The precipitate, if any was present, was discarded and the supernatant was precipitated with 50 mL of acetone and centrifugation at 12 krpm (29500 g) for 10 minutes at 17°C. The precipitate was dispersed in 10 mL of toluene. Subsequently the NCs were purified from excess ligands and synthesis byproducts by repeated (3 times) precipitation with acetone (2 volumetric equivalents) and centrifugation at 12 krpm for 1 minute at 17°C and dispersion in toluene. The solvent volume was reduced by factor 2 in each washing step. For the last dispersion 3 mL of toluene were used. The final concentration of the colloidal solution was 90 mg/mL.

1.3 Nanocrystal films

Substrates (z-cut quartz) were sonicated 2x in soap water for several minutes and rinsed with deionized water and dried with compressed air. They were then sonicated in ethanol and in acetone and dried with compressed air after each step. 60 µL of hexamethyldisilazane was drop cast onto the substrate, let to dry under ambient conditions. The substrates were then annealed on a hotplate 150 °C for 1 hour and let to cool down in a dust-free environment. Then, 60 µL of the NC solution were used for spin-coating. Spin coating parameters are pre-spinning 1 s, 500 rpm for 10 s and 2000 rpm for 1 min.

1.4 Solid state ligand exchange

For ligand exchange 0.0125 M (saturated) solutions of **2** in 1:1 anhydrous Methanol:Ethanol were prepared and stored over molecular sieves to counteract the hygroscopic nature of the

ligand. Freshly spin-coated films with lecithin ligands were subjected to ligand exchange by addition of 50 µL of the above described solution for 10 s and subsequent spin coating at 500 rpm for 10s and 2000 rpm for 1 minute. The thickness of the initial NC film is critical for the success of this method. Higher and lower concentrations of the NC colloidal solution lead to cracking and film dissolution respectively.

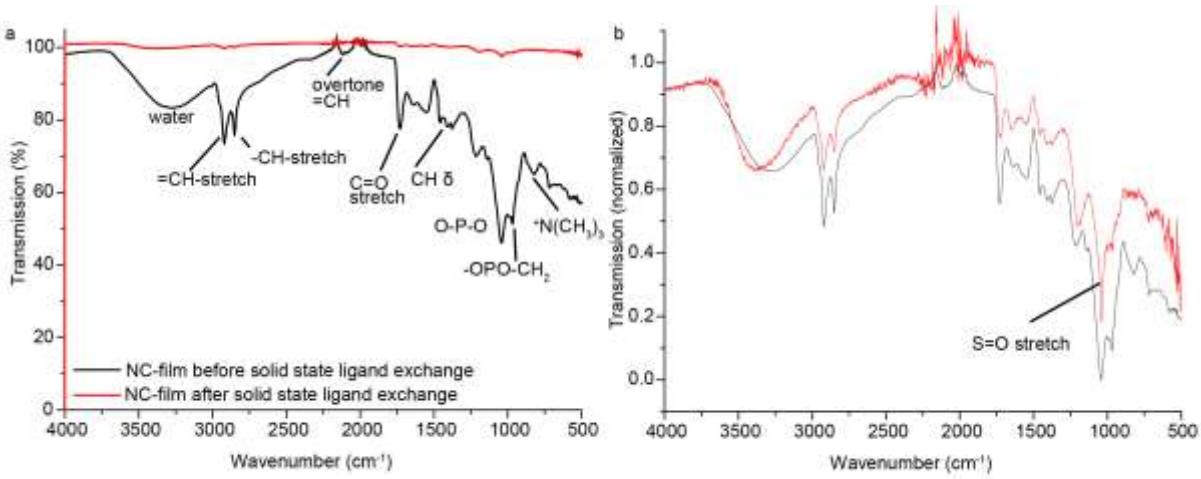

Figure S1. (a) FTIR spectrum of the film (lecithin covered $CsPbBr_3$ NCs) before and after solid state ligand exchange, clearly shows the reduction of the organics content. (b) the same spectra normalized to visualize the residual FTIR signals. While the samples typical to lecithin such as the phosphonate, carbonyle and terminal ammonium signals are reduced in intensity the S=O stretch is becoming dominant.

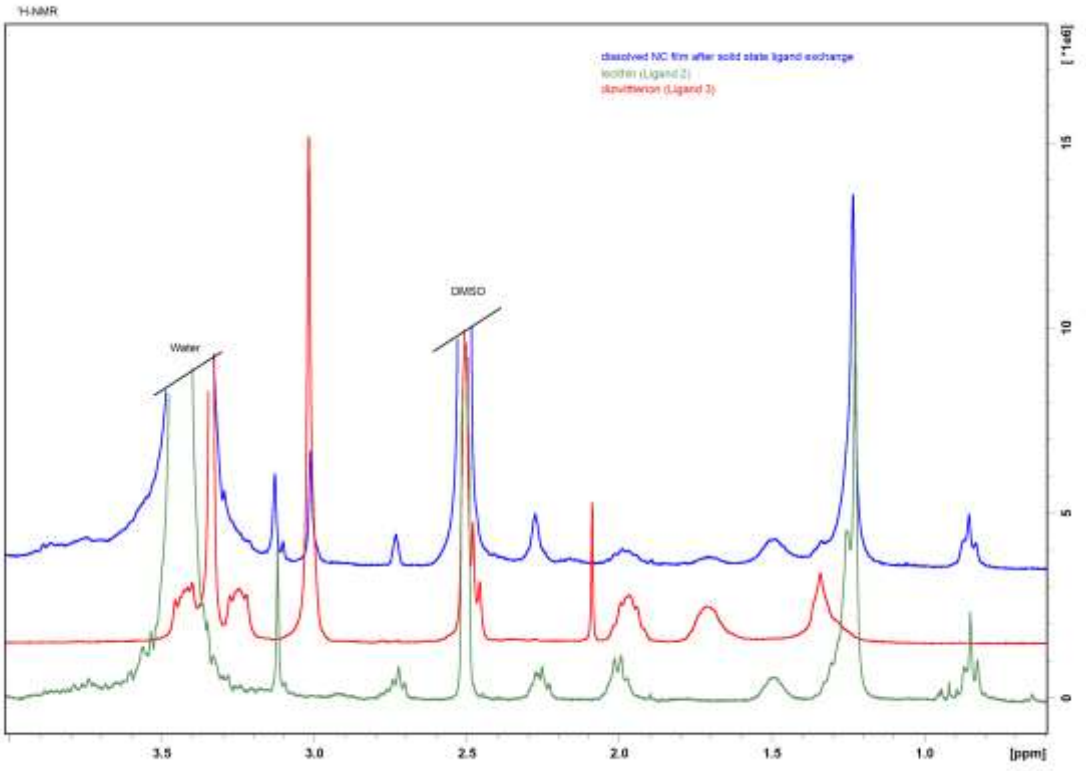

Figure S2. 1H-NMR of a dissolved film after solid state ligand exchange, with reference spectra of the ligand before exchange (lecithin, Ligand 2) and the ligand after exchange (Ligand 3). If the integral of the methyl groups at the ammonium (singlet above 3 ppm) are compared the new ligand makes up for 47% of the total ligand after ligand exchange. This result is less than what was expected based on FTIR probably due to incomplete penetration of the film by the ligand exchange solution.

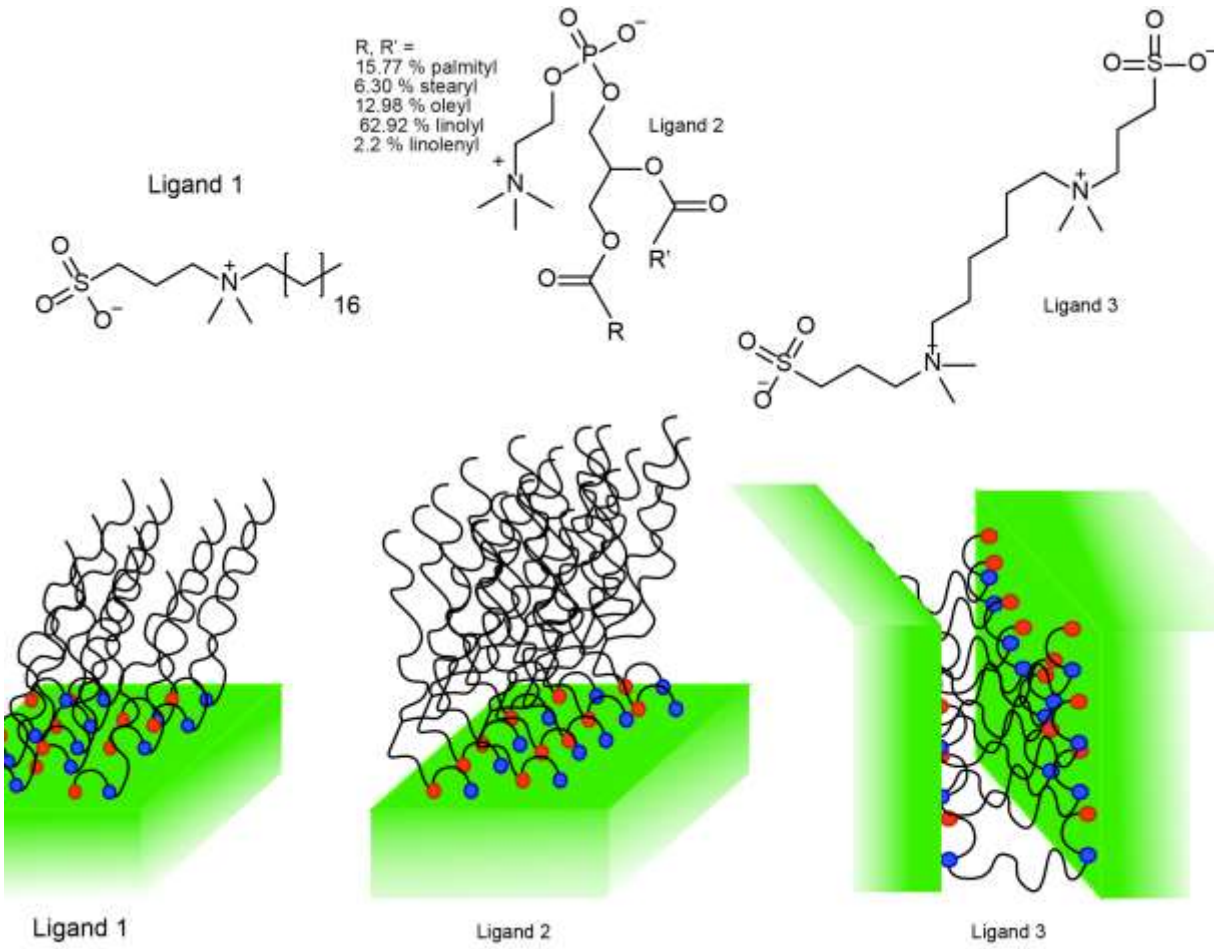

Figure S3. Illustration of the nanocrystal surfaces capped with ligands 1, 2 and 3.

Table S1. Sizes and PLQY of NCs in solution and after film deposition.

NC size	PLQY (solution)	PLQY (film)
6 ± 1(75)	67.0%	50.5%
7.5 ± 1(77)	74.8%	47.0%
10 ± 1(71)	74.8%	26.0%

1.5 Bulk polycrystalline films

The bulk polycrystalline $CsPbBr_3$ films were spin-coated using 100 µL of a 0.4 M solution of cesium bromide and lead bromide in dimethyl sulfoxide (DMSO). The solution was statically

spread onto the quartz substrates and spun at 4000 rpm for 40 s. An anti-solvent quench of 150 µL of chloroform was dropped onto the substrates after 37 s of the spin-coating process. The films were then annealed at 100 °C for 10 minutes.

2 Characterization

2.1 Materials characterization

TEM images were collected using Hitachi HT7700 microscope operated at 120 kV and using a Philips CM 12 microscope operating at 120 kV. TEM images were processed using Fiji. ()

NMR spectra were measured on a Bruker Avance DPX-300 spectrometer operating on a proton frequency of 300.13 MHz proton frequency and equipped with a BBFO-Z probe. For the organic synthesis product characterisation chemical shifts (δ) are reported in ppm relative to tetramethylsilane (δ = 0 ppm) using the residual solvent peaks as internal standard. Coupling constants (J) are reported in Hertz and multiplicity of a peak is specified with the following notation: s = singlet, d = doublet, t = triplet, m = multiplet, bs = broad singlet.

Fourier transform infrared (**FTIR**) spectra were measured by attenuated total reflectance (ATR). Spectra were recorded using Thermo Scientific Nicolet iS5 FTIR spectrometer.

Quantum Yield of solutions and films were measured with a Quantaurus-QY Absolute PL quantum yield spectrometer from Hamamatsu.

AFM images were collected using an Asylum MFP3D (Asylum Research and Oxford Instruments Co.) in AC (tapping) mode. Olympus AC240-TS silicon tips were used for topography measurements.

2.2 Steady-State Absorption

Refection and transmission spectra were measured using a Bruker 80v Fourier-transform infrared spectrometer with a tungsten halogen lamp source, a CaF beam splitter and a silicon

diode detector. Data was collected with a resolution of 4 cm^{-1}. A silver mirror was used as reflection reference and a blank quartz substrate was used as transmission reference. The reflectivity spectra were obtained from the measurement of reflected light from the front of the film with the aluminum mirror reflection measurement as reference. The reflectivity values were used to account for reflection losses of the photoexcitation in further experiments and correctly estimate the charge-carrier density.

2.3 Steady-State and Time-Resolved Photoluminescence

The excitation source was a 398 nm pulsed diode laser (PicoHarp, LDH-D-C-405M) operating at 500 kHz. The PL was collected in reflection geometry and coupled into a grating spectrometer (Princeton Instruments, SP-2558). Steady-state spectra were acquired with an iCCD (PIMAX4, Princeton Instruments) and time-resolved measurements were acquired in a Time Correlated Single Photon Counting (TCSPC) system (PicoHarp300). The measurements were performed under vacuum (pressure $<10^{-1}$ mbar).

3 Optical-Pump Terahertz-Probe (OPTP) Spectroscopy

Optical-Pump THz-Probe (OPTP) measurements were performed using a Spectra Physics Mai Tai-Empower-Spitfire Pro Ti:Sapphire regenerative amplifier. The amplifier generates 35 fs pulses centered at 800 nm at a repetition rate of 5 kHz. The optical pump excitation was obtained by frequency doubling the fundamental laser output through a BBO crystal, resulting in 400 nm pulses. THz probe pulses were generated by a spintronic emitter which was composed of 1:8nm of $Co_{40}Fe_{40}B_{20}$ sandwiched between 2 nm of Tungsten and 2 nm of Platinum, all supported by a quartz substrate. Detection of the THz pulses was performed using electro-optic sampling in a ZnTe crystal (0.2 mm (110)-ZnTe on 3 mm (100)-ZnTe). The FWHMs of the beams for the pump and THz pulses at the sample were measured to be

1.8 mm and 0.7 mm respectively. The sample, THz emitter and THz detector were held under vacuum (<10^{-2} mbar) during the measurements.

The effective charge-carrier mobility was extracted from the OPTP data using the method previously described by Wehrenfennig et al.[5] In brief, the sheet photo-conductivity, ΔS, of a material with a thickness much shorter than the wavelength of the THz radiation can be expressed as

$$\Delta S = -\epsilon_0 c(n_a + n_b)(\Delta T/T) \quad \text{(S1)}$$

where n_a and n_b are the THz refractive indices of the materials interfacing the perovskite layer at the front and rear respectively. The quantity ΔT/T is the ratio of the photo-induced change in THz electric field to the transmitted THz electric field in the dark. The initial number of photo-excited charge carriers N is given by

$$N = \varphi \frac{E\lambda}{hc}(1 - R_{pump})(1 - T_{pump}) \quad \text{(S2)}$$

with E being incident pump pulse energy, λ the excitation wavelength, φ the ratio of free charges created per photon absorbed, and R_{pump} and T_{pump} being the reflected and transmitted fractions of the pump beam intensity. These two equations can be used to extract the charge-carrier mobility μ through

$$\mu = \frac{\Delta S A_{eff}}{Ne} \quad \text{(S3)}$$

where A_{eff} is the effective area from the overlap of the pump and probe beams and *e* is the elementary charge. Substituting Equations S1 and S2 into Equation S3 we obtain

$$\varphi\mu = -\frac{\epsilon_0 c(n_a+n_b)(A_{eff})}{Ne\lambda(1-R_{pump})(1-T_{pump})}\left(\frac{\Delta T}{T}\right) \quad \text{(S4)}$$

from which the effective charge-carrier mobility φμ may be determined based on the pump beam parameters and the initial measured ΔT/T of the sample. Here, μ is the charge-carrier mobility, and φ is the charge-to-photon branching ration which is assumed to be unity at room temperature.

Charge-carrier mobility values were calculated based on the average of at least 10 measurements.

3.1 Charge carrier dynamics

The ΔT/T dynamics can be related to the decay of the charge carrier density over time n(t). The transients were modelled as described elsewhere with the rate equation

$$\frac{dn}{dt} = -k_1 n - k_2 n^2 - k_3 n^3 \quad \text{(S5)}$$

where k_1, k_2 and k_3 are the first, second and third order recombination rate constants, respectively.

The differential THz transmission ΔT/T is proportional to the evolution of charge-carrier population over time after photoexcitation according to

$$\mathrm{n(t)} = \varphi \cdot \mathrm{C} \cdot \left(\frac{\Delta T}{T}\right)(\mathrm{t}) \quad \text{(S6)}$$

where *C* is the proportionality factor between the immediate THz response and the absorbed photon density. Such response is not necessarily linear, in particular at very high fluences. When considering variable φ and *C*, Equation S5 becomes

$$\frac{dn}{dt} = -k_1 n - C\varphi k_2 n^2 - C^2 \varphi^2 k_3 n^3 \quad \text{(S7)}$$

We can determine *C* from the lower fluences measurements and confirming negligible nonlinear effects (for example, by observing no fluence dependence of the obtained effective mobilities). The recombination rate constants obtained by the fits will then be k_1 and the effective parameters $\varphi^2 k_3$ and φk_2 (See Wehrenfennig et al.[1] for more details). In the case of the NCs presented here, the presence of excitons could have a lower contribution to the THz response, which can be considered as $\varphi<1$.

The fluence dependent ΔT/T of the $CsPbBr_3$ NCs were fitted considering no contribution of k_1. This approximation is valid in this case because of the higher contribution of second and third order rates in the timescales and carrier densities in the OPTP experiments. To account

for the varying photogeneration density through the thickness of the film, the fit routine takes into account the exponential charge density profile created by the excitation light by dividing the sample into 50 equally thick slices. The decay is computed individually for each slice and then added together to result in the observed OPTP decay. The complete dataset with various fluences was globally fitted, allowing k_2 and k_3 to vary. The photon-to-charge parameter φ was kept close to 1 but allowed to fluctuate in order to account for possible variations of charge-carrier population resulting from laser power fluctuations.

The first order rate constant k_1 was fixed to zero for the NCs dynamics, as discussed in the main text. k_2 and k_3 were globally fit to the fluence dependence set of OPTP transients.

3.2 THz photoconductivity spectra

The frequency dependence of the photoconductivity of $CsPbBr_3$ NCs and bulk film was taken at fluence 40 μJ/cm^2 at 20 ps after photoexcitation. As described in the main text, the spectra were simulated with the Drude model, which describes the photoconductivity σ as

$$\sigma(\omega) = \frac{Ne^2}{m^*}\frac{i}{\omega+i\gamma} \quad \text{(S8)}$$

where m^* is the charge carrier effective mass and γ is the scattering rate, which relates to the mobility μ by

$$\mu = \frac{e}{m^*\gamma} \quad \text{(S9)}$$

The simulation of the Drude spectra were obtained from the calculated photoexcitation density, fixing the mobility to the value measured experimentally and considering m^* as 0.15 m_e.

For the case of the NCs, where the spectra strongly deviate from the Drude model, the Drude-Smith model was also considered. The Drude-Smith model is a phenomenological adaptation of the Drude model that can account for scattering in preferential directions. The Drude-Smith expression for photoconductivity is given by

$$\sigma(\omega) = \frac{Ne^2}{m^*}\frac{i}{\omega+i\gamma}\left[1+\sum_{p=1}^{\infty}\frac{c_p}{(1-i\omega/\gamma)^p}\right] \quad \text{(S10)}$$

where γ_{DS} is the Drude-Smith scattering rate and c_p is the fraction of the carriers initial velocity retained after scattering event p. The infinite summation is usually truncated after the first term, p = 1 (i.e. single-scattering approximation).[6]

The simulated Drude-Smith spectra (dashed line in Figure 4 of the main text) was obtained fixing c_p to -1 and the intrinsic mobility to 400 cm^2/Vs, which is the theoretical upper limit when only Frohlich interactions with longitudinal phonons are operational.[7,8] The effective mass m^* was fixed to 0.15 m_e and the carrier population N was allowed to fluctuate in the fit routine from the initial estimated number of absorbed photons.

4 Charge-carrier density in isolated crystals

To take into account the spatial distribution of carrier population across the thickness of the film, we considered a Beer-Lambert profile of light intensity. The total average carrier density in the films was calculated based on the density of absorbed photons at each depth point through the film. Then the average carrier density was multiplied by the average volume of the NCs to give the average number of photoexcitations (i.e. excitons or electron-hole pairs) per NC at each depth position. Figures S1, S2 and S3 show the calculated density profiles for the three sizes of NCs at fluences employed during the PL and OPTP experiments.

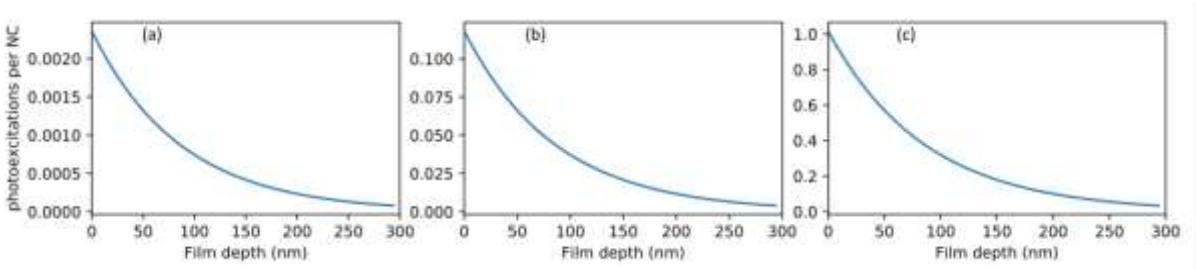

Figure S4. Estimated number of photoexcitations per NC for the 6 nm $CsPbBr_3$ NC (a) at 100 nJ/cm^2, the highest fluence employed in the PL dynamics measurements; (b) at 2 $\mu J/cm^2$ the lowest fluence employed in the OPTP measurements; and (c) at 20 $\mu J/cm^2$.

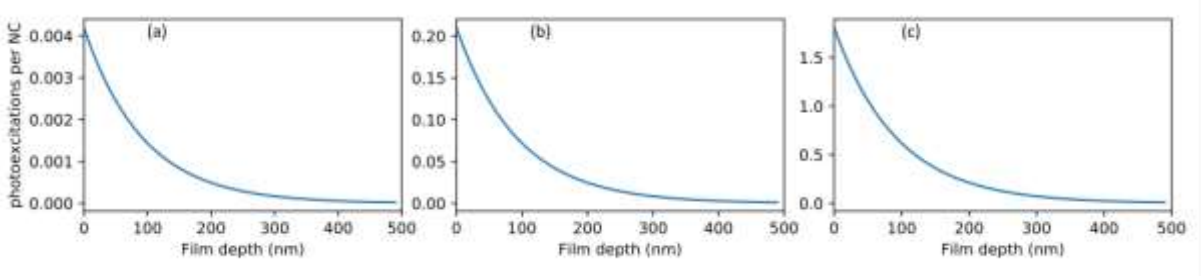

Figure S5. Estimated number of photoexcitations per NC for the 7.5 nm $CsPbBr_3$ NC (a) at 100 nJ/cm^2, the highest fluence employed in the PL dynamics measurements; (b) at 2 µJ/cm^2 the lowest fluence employed in the OPTP measurements; and (c) at 20 µJ/cm^2.

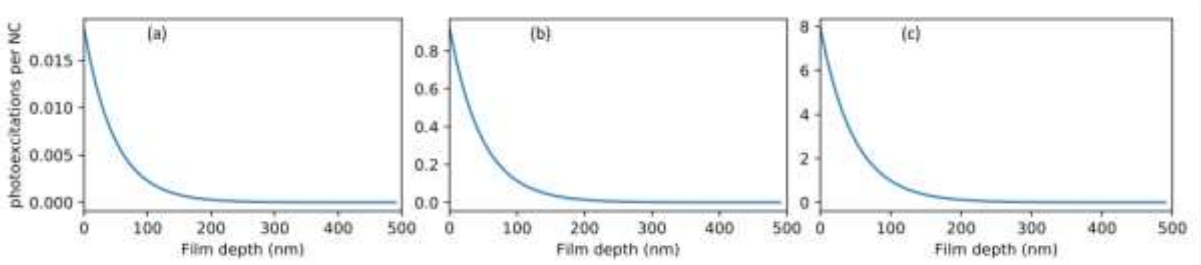

Figure S6. Estimated number of photoexcitations per NC for the 10 nm $CsPbBr_3$ NC (a) at 100 nJ/cm^2, the highest fluence employed in the PL dynamics measurements; (b) at 2 µJ/cm^2 the lowest fluence employed in the OPTP measurements; and (c) at 20 µJ/cm^2.

5 XRD analysis

The samples were mounted on a rotating sample holder in air and at room temperature and measurements were performed using an X-ray diffractometer Panalytical X'Pert Pro, Cu-Kα radiation at λ = 1.54 Å, operating at 40 kV and 40 mA. The step size was 0.008°, 0.4 second per step for the 7.5 and 6 nm NCs, and for the more detailed analysis (Williamson-Hall and Pawley fit), the 10 nm NC and the bulk polycrystalline films were measured with a step size of 0.002°, 1 second per step. The peak positions were corrected for sample tilt by using the z-cut quartz peaks at 16.433° and 50.66° as a reference.

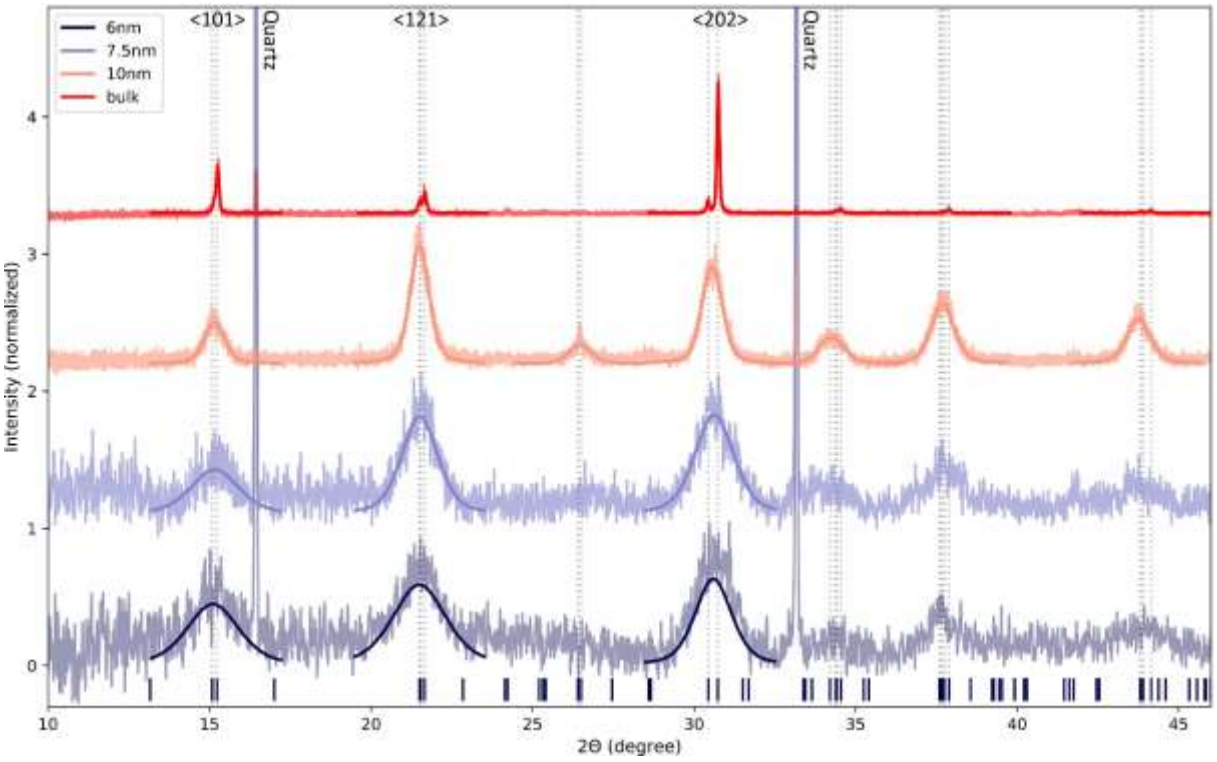

Figure S7. Normalized XRD diffraction patterns for the $CsPbBr_3$ NCs and polycrystalline films. An offset was added for visualization. The solid lines are fits of the peaks with Pseudo-Voigt functions. A superposition of two peaks was used when two peaks could be resolved and in accordance with the expected peak positions from the reference pattern for orthorhombic $CsPbBr_3$ (as marked by lines at the bottom of the figure).

In order to properly analyse the position and broadening of the diffraction peaks, we must take into account the crystalline phase and peak superpositions. It has been determined that $CsPbBr_3$ NCs fabricated from colloidal synthesis adopt an orthorhombic structure, as does the bulk material.[9] According to the expected diffraction pattern for orthorhombic $CsPbBr_3$,[6] many of the peaks that appear as a single broad feature correspond to two or more diffraction indexes. As a first step of the analysis we fitted the peaks individually considering a superposition of two Pseudo-Voigt functions. The superposition was considered in accordance to the expected peak separation and the size related broadening and instrument response limitations. This was done in order to avoid overestimation of linewidths and errors

in peak positions in the cases where size-related broadening and instrument response would allow to resolve the peak separation, which would result in the overestimation of Δd between samples.

We then calculated the d-spacings for the most prominent reflections. The d-spacings were calculated from peak positions according to Bragg's Law:

$$2d \cdot sin(\Theta) = n \tag{S11}$$

Figure S8 shows the d-spacings obtained for (101), (121) and (202) peaks. We noticed that the bulk perovskite shows slightly but consistently shorter plane distances than the NCs (i.e. Δd = 0.04, 0.01 and 0.01 Å for (101), (121) and (202) planes, respectively).

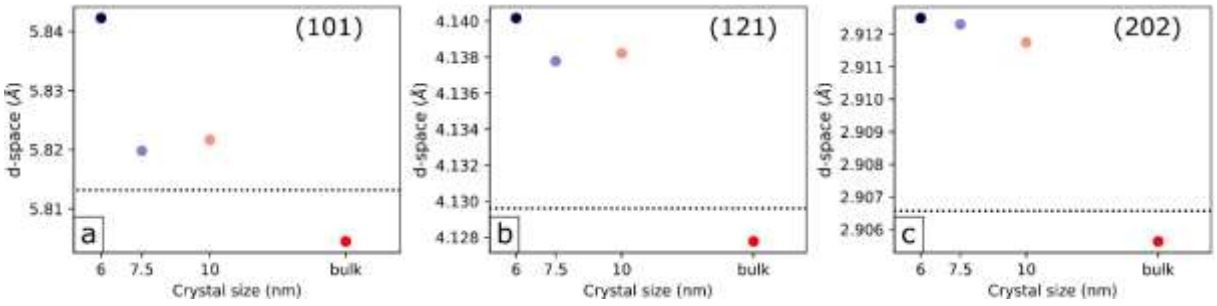

Figure S8. Crystal size dependence on d-spacing for reflections (101), (121) and (202). The dotted line shows the d-space obtained from the crystallographic information reported by Stoumpos et al.[6]

5.1 Williamson-Hall plots

We then used the diffraction patterns of the 10 nm NCs and the bulk polycrystalline films for further analysis, as these presented better signal-to-noise ratio and lower contribution from crystal size broadening. We first corrected the fitted full width at half maxima (FWHM) of the peaks for the instrument response broadening, which was calculated from a quadratic fit to the diffraction pattern of a silicon reference sample (Figure S9).

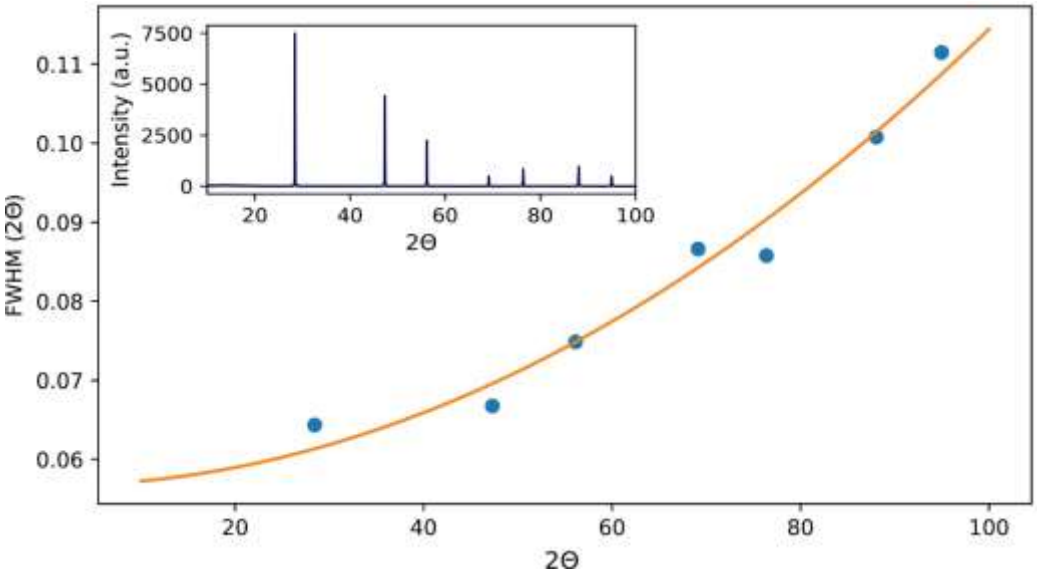

Figure S9. Peak broadening as a function of position (2Θ) taken from the diffraction pattern of a silicon reference (inset). Orange line is a quadratic fit used to obtain instrument response broadening.

The corrected FWHM and the fitted peak positions were used in the Williamson-Hall plots. The formula that accounts for size and microstrain related broadening according to the peak position is given by

$$\beta = \frac{K\lambda}{D \cdot cos(\Theta)} + 4\epsilon \cdot tan \tag{S12}$$

where *D* is the crystallite size, Θ is the Bragg angle, β is the FWHM in radians and *K* is the shape factor that can usually be assumed to be 0.9. This can be rearranged to

$$\beta \cdot cos(\Theta) = \frac{K\lambda}{D} + 4\epsilon \cdot sin \tag{S13}$$

We can then plot βcos(Θ) as a function of sin(Θ), and the linear regression obtained from the peaks allow us to determine the crystallite size from the intercept and the microstrain from the slope.

As can be seen in Figure S10, the crystal size obtained from the plots are close to the size obtained from TEM and AFM measurements on the samples. Furthermore, the microstrain

contribution is very low, which indicates a good crystalline quality with little distortion related to defects and impurities.

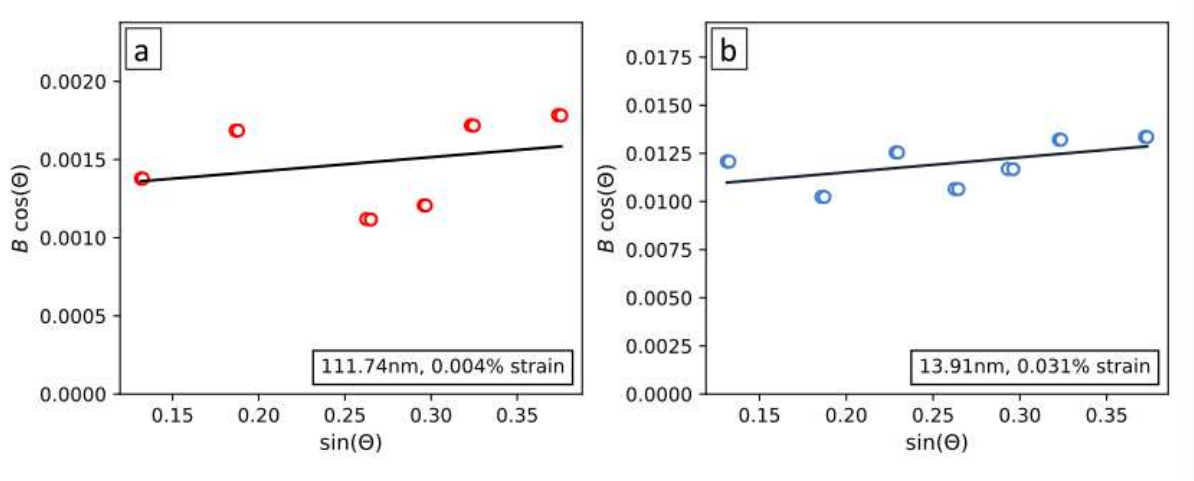

Figure S10. Williamson-Hall plots for (a) polycrystalline CsPbBr3 films and (b) nanocrystals (10 nm).

5.2 Pawley fit

As a further step in the analysis we then performed a Pawley fit using the analysis software PANalytical X'Pert Pro. We have used the reference card for orthorhombic $CsPbBr_3$ and excluded from the analysis the peaks corresponding to the quartz substrate and the predicted peaks that were not visible in the experimental data. The Cagliotti parameters, the peak intensities and broadening were allowed to vary, while the peak positions were fitted by refining the dimensions of the unit cell. Figure S11 shows the fitted patterns for the 10 nm NCs and the bulk polycrystalline $CsPbBr_3$. Table S2 shows the values obtained from the fit compared to the values reported by Stoumpos et al.[10] The fitted dimensions of the unit cell show a small but consistent constriction of the lattice in the bulk material compared to the NCs. This observation, combined with the negligible contribution of microstrain, suggests a uniform lattice expansion in the colloidally synthesized NCs.

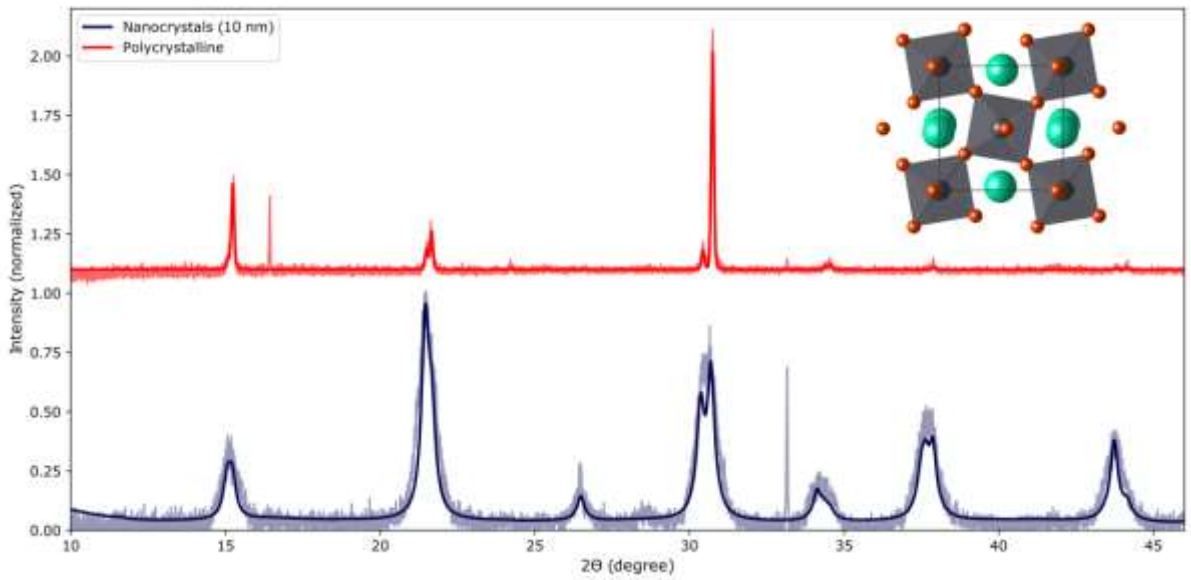

Figure S11. Normalized XRD diffraction patterns for the $CsPbBr_3$ nanocrystals of size 10 nm (in blue) and polycrystalline (in red) films. An offset was added for visualization. The solid lines are Pawley fits to the experimental data based on the reference pattern for orthorhombic $CsPbBr_3$ (inset) as reported by Stoumpos et al.[6]

Table S2. Lattice parameters for the orthorrhombic unit cell obtained from the Pawley fit.

lattice parameter (Å)	Stoumpos et al.[6]	NC (10 nm)	Polycrystalline
a	8.2440(6)	8.27(3)	8.246(5)
b	11.7351(11)	11.77(7)	11.750(6)
c	8.1982(8)	8.19(1)	8.198(5)

6 Supplementary figures

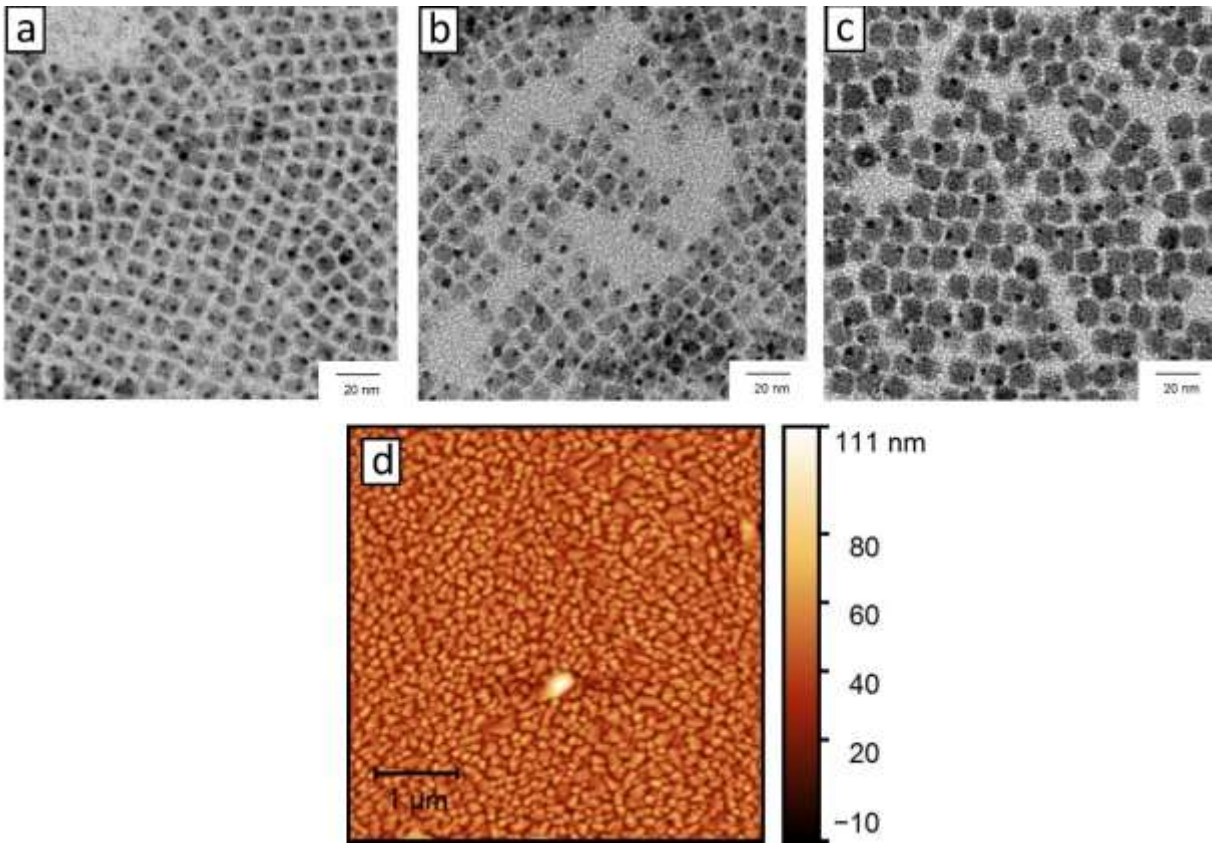

Figure S12. Transmission electron microscopy (TEM) images of the (a) 6 nm, (b) 7.5 nm and (c) 10 nm CsPbBr3 NCs; (d) topography of the bulk polycrystalline CsPbBr3 film measured by atomic force microscopy (AFM).

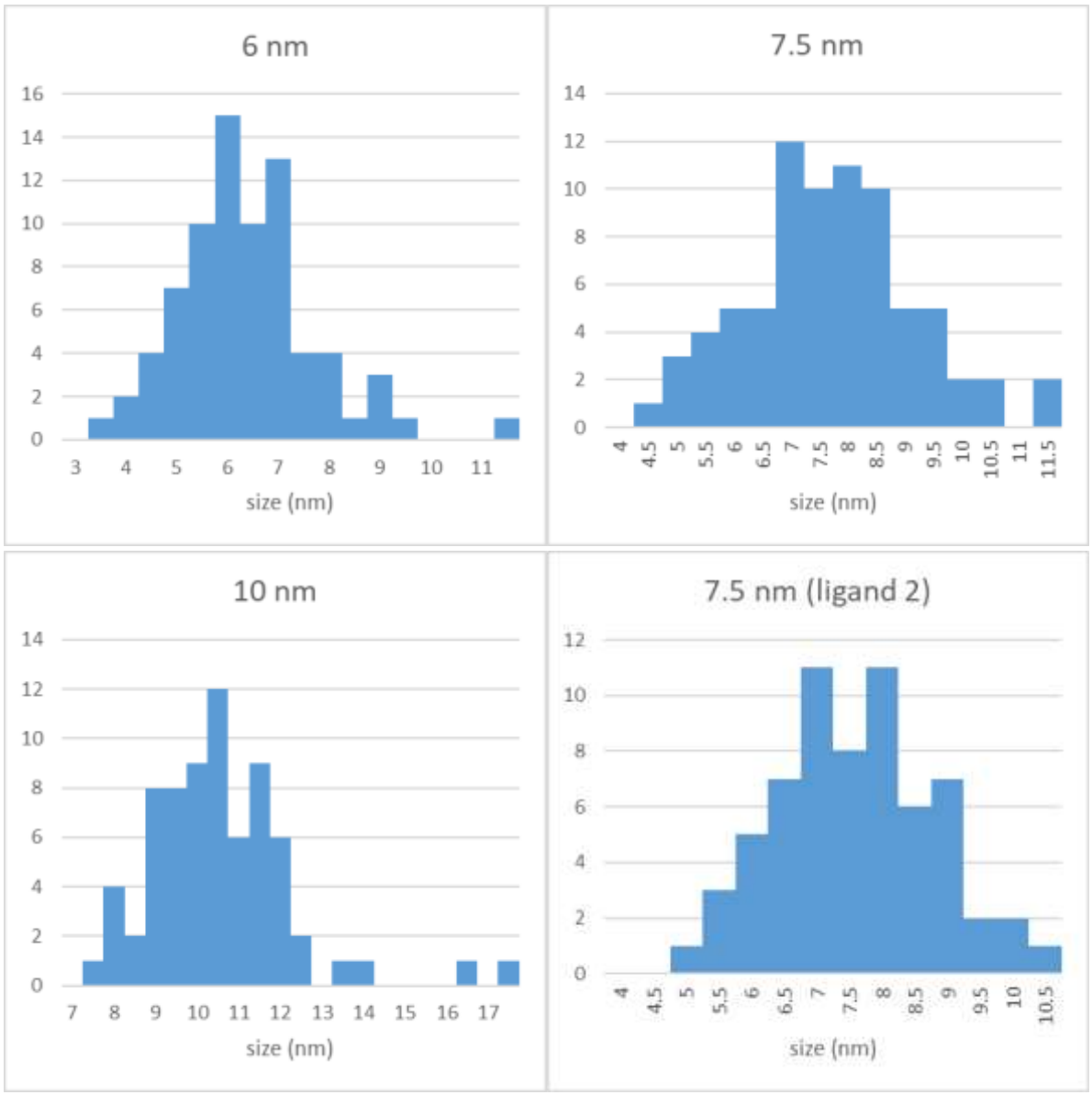

Figure S13. Size distribution histograms for the 6 nm, 7.5 nm and 10 nm NCs with ligand 1 and 7.5 nm NC with ligand 2.

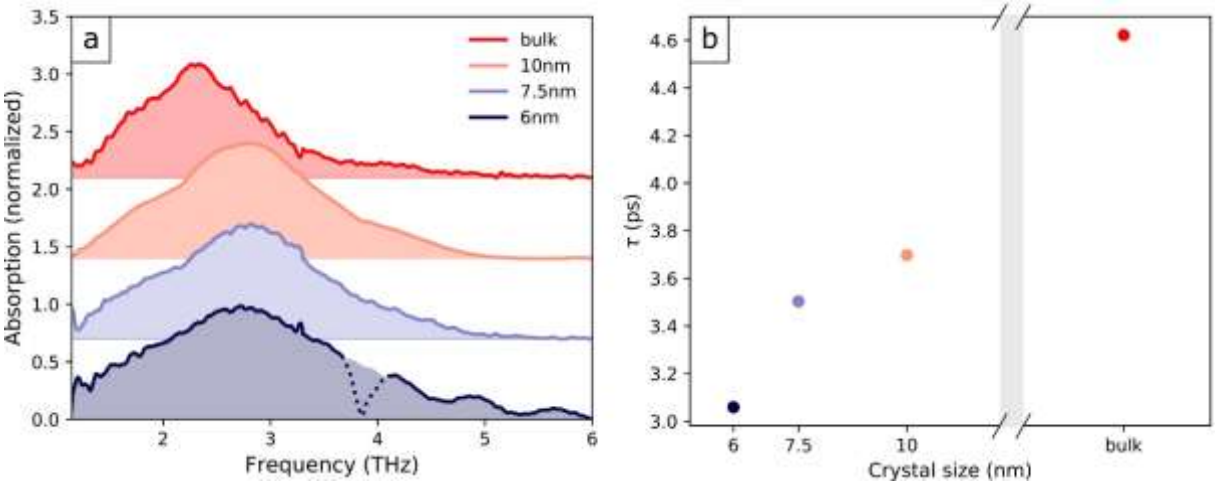

Figure S14. THz absorption in dark, taken at room temperature with a bolometer (a) of $CsPbBr_3$ nanocrystals of size 10 nm, 7.5 nm and 6 nm, and polycrystalline films (offset was added for clarity). Dotted line in the 6 nm NC spectrum is an artefact caused by the quartz absorption. (b) estimated phonon lifetimes based on the spectral linewidths.

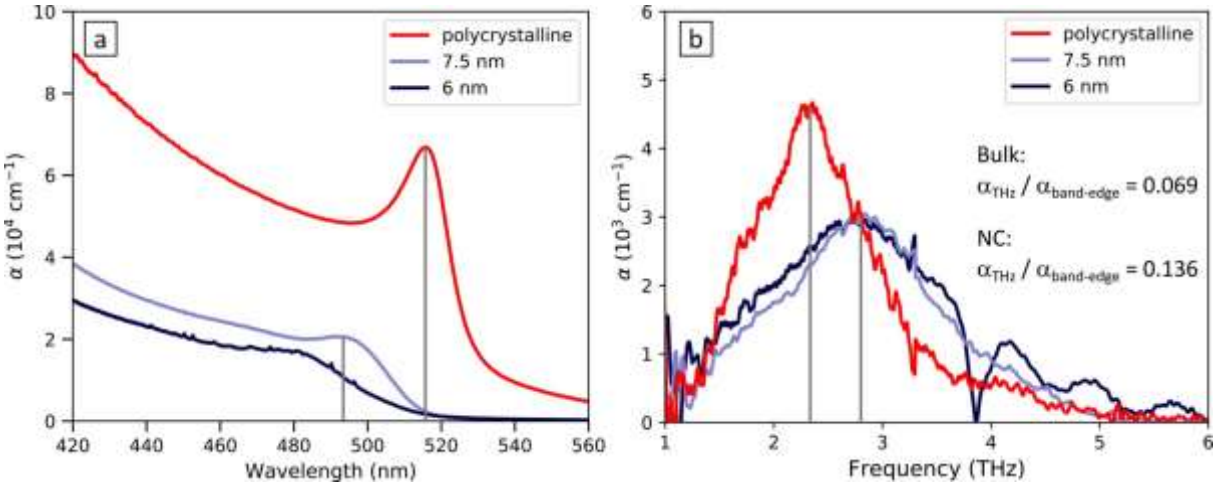

Figure S15. (a) Absorption coefficient α (obtained from optical density divided by film thickness) of bulk polycrystalline and nanocrystalline CsPbBr3 in the visible range and (b) in the THz range. The 10 nm NC film was excluded because of uncertainties related to high optical density and film roughness. Although the absolute values are not accurate due to the presence of ligands and film inhomogeneity, we can compare the relative α, i.e., the α at the maximum of the THz absorption spectra divided by the α at the band-edge (positions marked

with a grey line). What we can observe is that the relative α for phonon absorption in the THz region in the NC films is higher by a factor of 2.

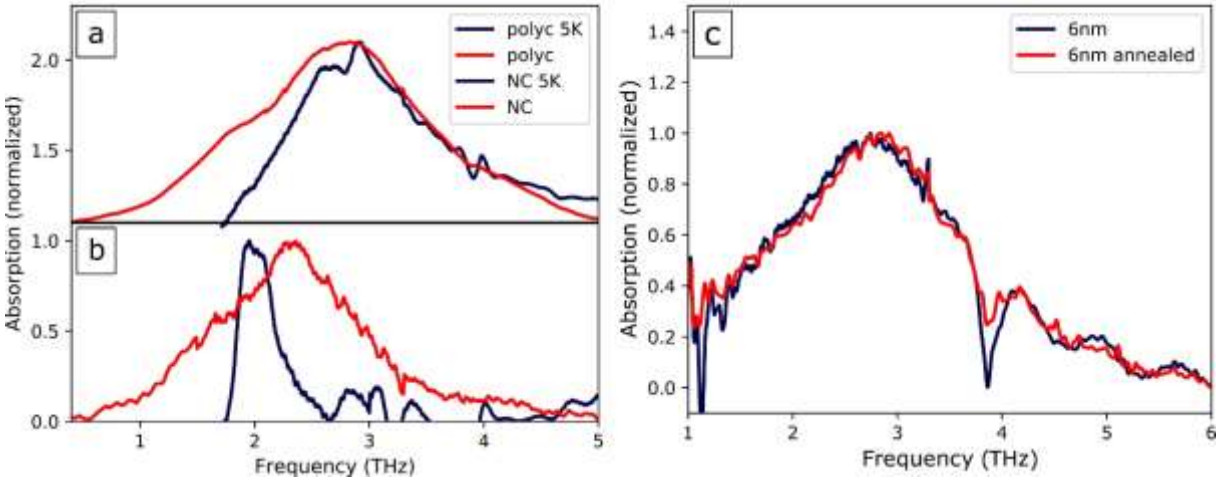

Figure S16. THz absorption in dark, at room temperature (red) and at 5K (dark blue) of (a) $CsPbBr_3$ nanocrystals of size 10 nm (in blue) (b) and polycrystalline (in red) films. (c) THz absorption in dark, at room temperature, of 6 nm nanocrystals deposited in Quartz, before and after annealing for 150 °C for 10 minutes.

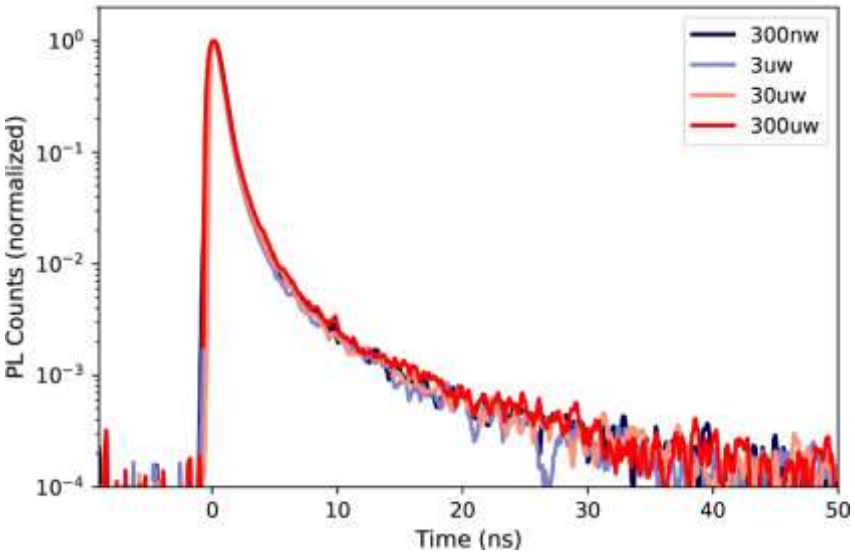

Figure S17. PL dynamics of $CsPbBr_3$ (7.5 nm) deposited on Quartz, showing no dependence on excitation fluence.

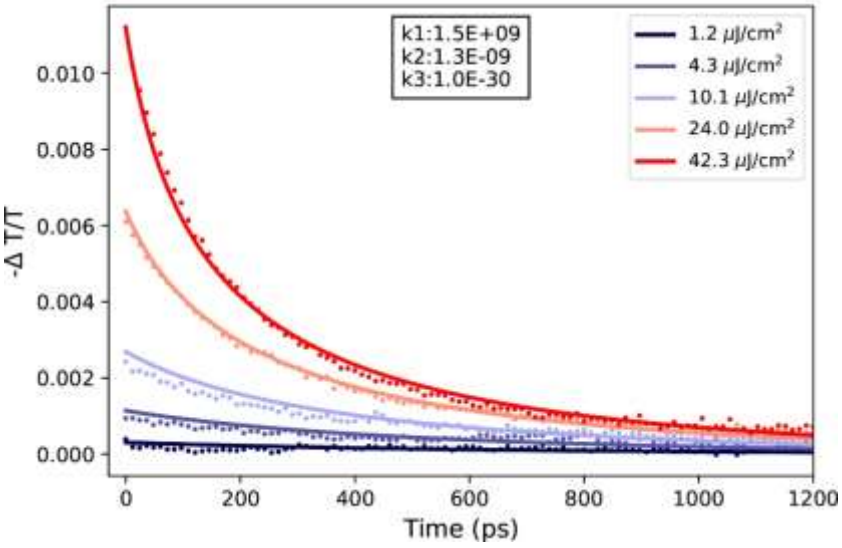

Figure S18. OPTP dynamics of $CsPbBr_3$ polycrystalline film. Dots are experimental data and solid lines are fits to the fluence dependence with the rate equation system described in Section 1.5.

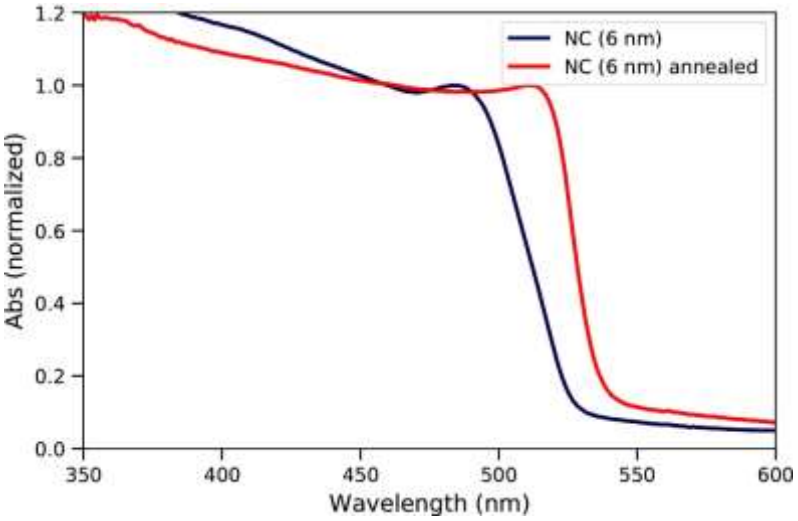

Figure S19. Absorption spectra of $CsPbBr_3$ 6 nm nanocrystals deposited in Quartz, before and after annealing for 150 °C for 10 minutes.

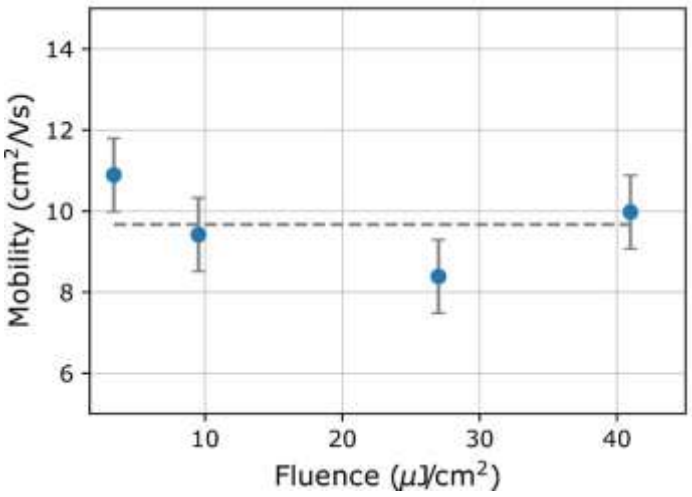

Figure S20. Effective THz mobilities of bulk polycrystalline $CsPbBr_3$ at different fluences, showing no clear dependence.

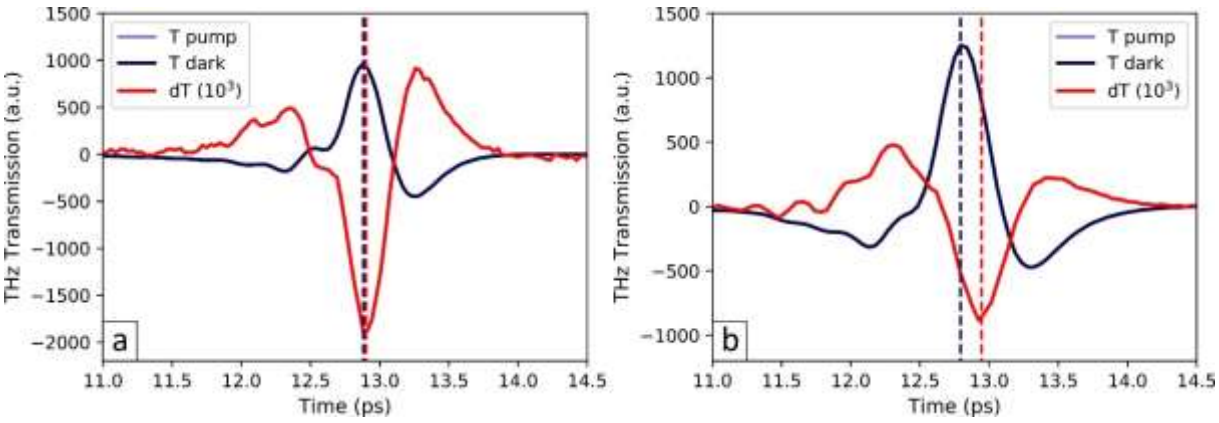

Figure S21. Time domain THz pulse transmission through (a) of bulk polycrystalline $CsPbBr_3$ and (b) 10 nm NCs. Photoexcited differential transmission is plotted in red and evidences the shift of the THz peak in the NCs due to a photoinduced change in refractive index.

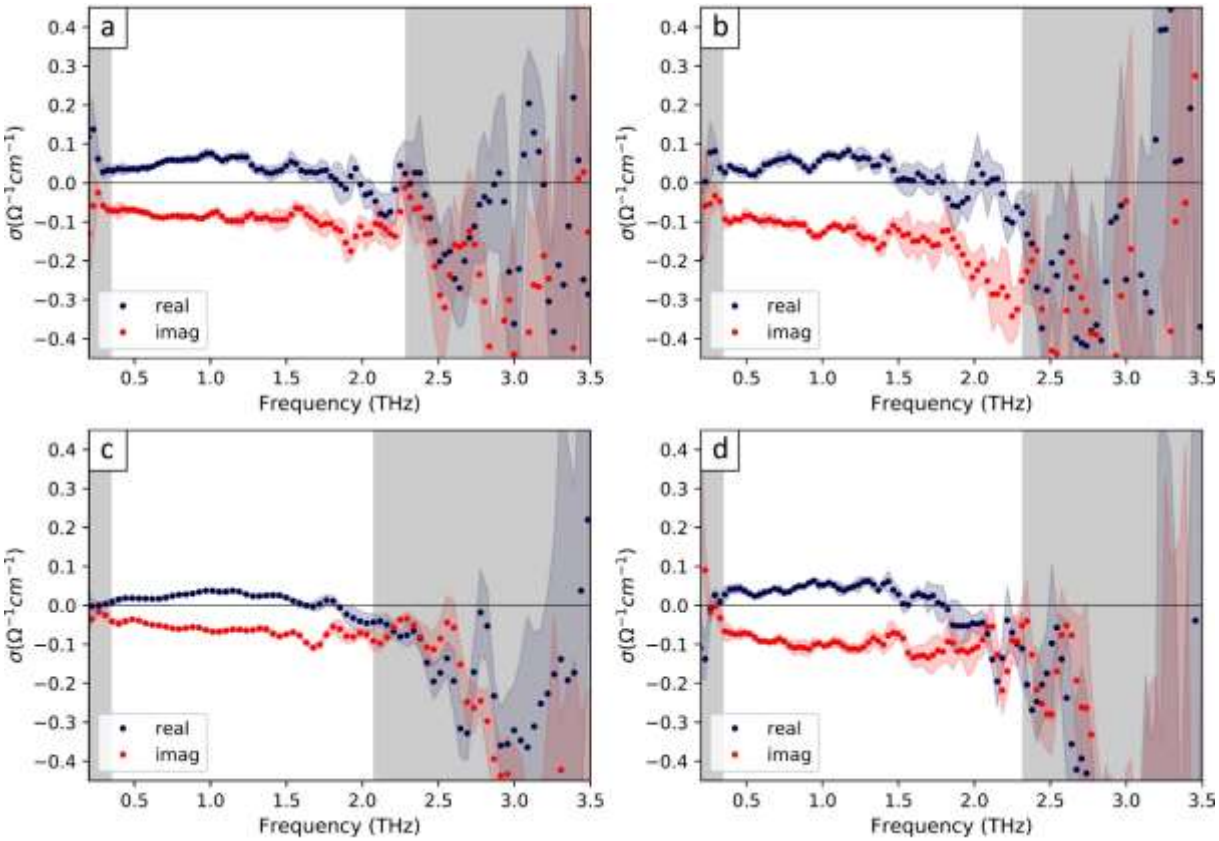

Figure S22. Real (dark blue) and imaginary (red) parts of THz photoconductivity spectra of (a) 6 nm, (b) 7.5 nm (ligand 1), (c) 7.5 nm (ligand 2) and (d) 7.5 nm (ligand 3) $CsPbBr_3$ nanocrystals deposited in Quartz.

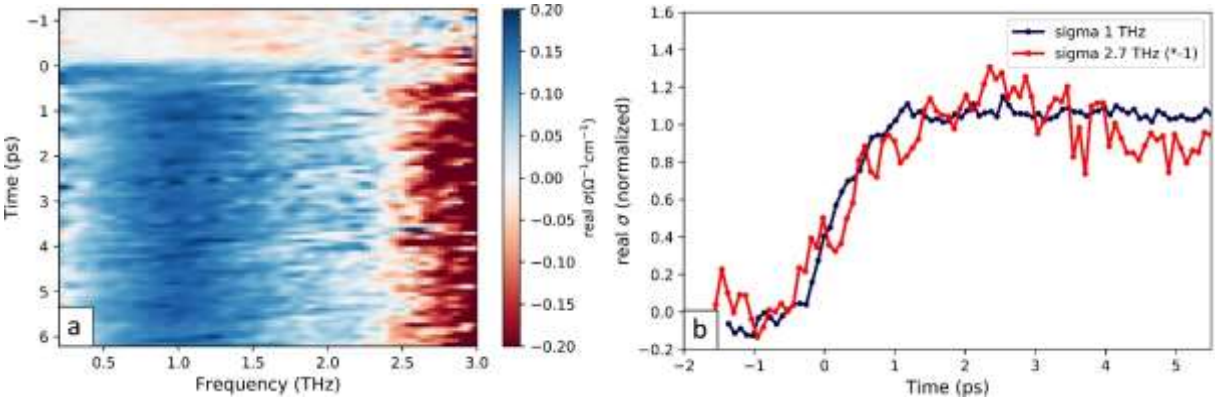

Figure S23. (a) Time resolved THz photoconductivity (real part) of nanocrystalline $CsPbBr_3$ deposited on Quartz (average size 10 nm); (b) Dynamic profile at 1 and 2.7 THz (normalized). The 2.7 THz dynamic trace was multiplied by -1.

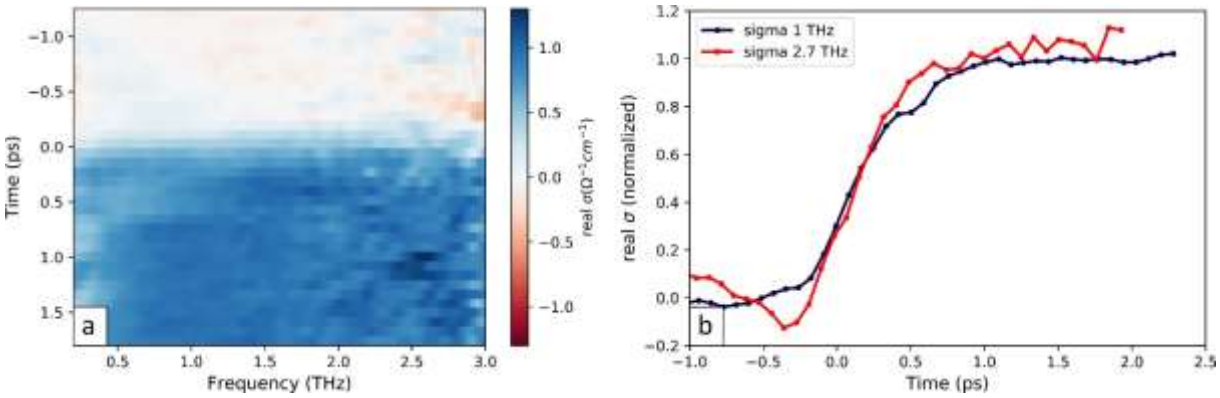

Figure S24. (a) Time resolved THz photoconductivity (real part) of bulk polycrystalline $CsPbBr_3$ deposited on Quartz; (b) Dynamic profile at 1 and 2.7 THz (normalized).

References

[1] M. E. Kateb, E. T. de Givenchy, A. Baklouti, F. Guittard, *J. Colloid Interface Sci.* **2011**, *357*, 129.

[2] F. Krieg, S. T. Ochsenbein, S. Yakunin, S. ten Brinck, P. Aellen, A. Süess, B. Clerc, D. Guggisberg, O. Nazarenko, Y. Shynkarenko, S. Kumar, C.-J. Shih, I. Infante, M. V Kovalenko, *ACS Energy Lett.* **2018**, *3*, 641.

[3] J. Maes, L. Balcaen, E. Drijvers, Q. Zhao, J. De Roo, A. Vantomme, F. Vanhaecke, P. Geiregat, Z. Hens, *J. Phys. Chem. Lett.* **2018**, *9*, 3093.

[4] F. Krieg, Q. K. Ong, M. Burian, G. Rainò, D. Naumenko, H. Amenitsch, A. Süess, M. J. Grotevent, F. Krumeich, M. I. Bodnarchuk, I. Shorubalko, F. Stellacci, M. V. Kovalenko, *J. Am. Chem. Soc.* **2019**, 141, 19839.

[5] C. Wehrenfennig, G. E. Eperon, M. B. Johnston, H. J. Snaith, L. M. Herz, *Adv. Mater.* **2014**, *26*, 1584.

[6] H. J. Joyce, J. L. Boland, C. L. Davies, S. A. Baig, M. B. Johnston, *Semicond. Sci. Technol.* **2016**, *31*, 103003.

[7] S. Poncé, M. Schlipf, F. Giustino, *ACS Energy Lett.* **2019**, *4*, 456.

[8] M. Sendner, P. K. Nayak, D. A. Egger, S. Beck, C. Müller, B. Epding, W. Kowalsky, L. Kronik, H. J. Snaith, A. Pucci, R. Lovrinčić, *Mater. Horizons* **2016**, *3*, 613.

[9] P. Cottingham, R. L. Brutchey, *Chem. Commun. Chem. Commun* **2016**, *5246*, 5246.

[10] C. C. Stoumpos, C. D. Malliakas, J. A. Peters, Z. Liu, M. Sebastian, J. Im, T. C. Chasapis, A. C. Wibowo, D. Y. Chung, A. J. Freeman, B. W. Wessels, M. G. Kanatzidis, *Cryst. Growth Des.* **2013**, *13*, 2722.